20961

NATIONAL LIBRARY
OTTAWA

CANADA

BIBLIOTHÈQUE NATIONALE
OTTAWA

NAME OF AUTHOR..... Jun Amano .....

TITLE OF THESIS... Field Ion Microscopy of ...
... Field Corrosion of Tungsten ...

.....

UNIVERSITY..... of Alberta .....

DEGREE FOR WHICH THESIS WAS PRESENTED..... M.Sc. .....

YEAR THIS DEGREE GRANTED..... 1974 .....

Permission is hereby granted to THE NATIONAL LIBRARY OF CANADA to microfilm this thesis and to lend or sell copies of the film.

The author reserves other publication rights, and neither the thesis nor extensive extracts from it may be printed or otherwise reproduced without the author's written permission.

(Signed)..... Jun Amano ...

PERMANENT ADDRESS:

... 19-5 Higashimine-machi
... Ota-ku, Tokyo., Japan

.....

DATED.. Nov. 28 1973

NL-91 (10-68)

THE UNIVERSITY OF ALBERTA

FIELD ION MICROSCOPY OF FIELD CORROSION OF TUNGSTEN

by

© JUN AMANO

A THESIS

SUBMITTED TO THE FACULTY OF GRADUATE STUDIES

AND RESEARCH IN PARTIAL FULFILLMENT OF THE REQUIREMENTS

FOR THE DEGREE OF MASTER OF SCIENCE

DEPARTMENT OF ELECTRICAL ENGINEERING

EDMONTON, ALBERTA

SPRING, 1974

THE UNIVERSITY OF ALBERTA

FACULTY OF GRADUATE STUDIES AND RESEARCH

The undersigned certify that they have read, and recommend to the Faculty of Graduate Studies and Research, for acceptance, a thesis entitled FIELD ION MICROSCOPY OF FIELD CORROSION OF TUNGSTEN submitted by JUN AMANO in partial fulfilment for the requirements for the degree of Master of Science.

Supervisor

Date November 23, 1973

ABSTRACT

The electrodeposition of zinc and its post-deposition oxidation on field ion microscope tungsten tip specimens were carried out by using a non-bakeable all glass high vacuum field ion microscope. It was impossible to observe the zinc and zinc-oxide thin films by using this field ion microscope; instead, field corrosion of tungsten tip was observed.

Two types of field corrosion were observed. When the main reactant was only oxygen, corrosion was observed at the edges of the imaging area and extensive changes in surface topography were not observed. On the other hand when the water molecules were presented, corrosion occurred over the whole imaging area and consequently extensive changes in surface topography were observed as a result of corrosion induced reactions in local radii of curvature of tip specimens.

ACKNOWLEDGMENT

The research described in this thesis was carried out at the Department of Electrical Engineering, the University of Alberta, under the supervision of Dr. R.P.W. Lawson, to whom the author wishes to acknowledge his indebtedness for advice.

The contributions of the people in the High Vacuum Laboratory of the Department of Electrical Engineering, in the form of fruitful discussions, and especially the help of Mr. B. Gregov, in carrying out experiments, are sincerely acknowledged.

The author also wishes to thank the National Research Council of Canada and the University of Alberta for financial support.

Finally, the author wishes to express his appreciation to his friends, Ms. D. Touchings and Mr. M. Roth, whose understanding has been a constant source of encouragement.

TABLE OF CONTENTS

CHAPTER		PAGE
1	INTRODUCTION	1
2	PRINCIPLES OF FIELD ION MICROSCOPE	4
	2.1 Basic principles	4
	2.2 Field ionization	6
	2.3 Field evaporation	10
	2.4 Field and stress	11
3	FIELD CORROSION	14
	3.1 Mechanism of field corrosion	14
4.	GROWTH AND STRUCTURE OF ELECTRODEPOSITS	17
	4.1 Nucleation and growth of electrodeposits	17
	4.2 Formation and structure of zinc and zinc-oxide	22
5.	EXPERIMENT	25
	5.1 Microscope chamber	25
	5.2 Vacuum system	26
	5.3 Gas handling plant	27
	5.4 Specimen preparation	29
	5.5 Photography and image intensification	31
	5.6 Experimental procedure	31

CHAPTER		PAGE
6	RESULTS AND DISCUSSION	33
	6.1 The effect of the atmospheric adsorption	33
	6.2 The effect of deposition solution	38
	6.3 The effect of electrodeposition	43
	6.4 The effect of post-deposition oxidation	51
7	CONCLUSIONS	58
	7.1 Results	58
	7.2 Suggestions for further work	59
REFERENCES		60

LIST OF FIGURES

Figure	Description	Page
2.1	Field ion micrograph of a tungsten tip of approximately 500Å	5
2.2	Schematic diagram of a field ion microscope	7
2.3	Potential diagrams of an electron in field ionization	7
2.4	The variation of the electric field with the distance from the tip apex	13
2.5	The variation of stress with the distance from the tip apex	13
4.1	Simple Terrace-Ledge-Kink model	19
4.2	Alternative and consecutive steps in lattice building	21
5.1	Microscope chamber	26
5.2	FIM system diagram	28
6.1 a-b	Tungsten surface, (a) before atmospheric adsorption, (b) after atmospheric adsorption	35
6.1 c-d	Same surface, (c) and (d) after atmospheric adsorption	36
6.1 e-f	Same surface, (e) and (f) after atmospheric adsorption	37
6.2 a-b	Tungsten surface, (a) before immersion to deposition solution, (b) after immersion	40

Figure	Description	Page
6.2 c-d	Same surface, (c) and (d) after immersion	41
6.3 a-b	Tungsten surface, (a) before electrodeposition, (b) after electrodeposition	44
6.3 c-d	Same surface, (c) and (d) after electrodeposition	45
6.3 e-f	Same surface, (e) and (f) after electrodeposition	46
6.4 a-e	Tungsten surface, (a) before electrodeposition (b)-(e) after electrodeposition	47
6.4 f-j	Same surface, (f)-(j) after electrodeposition	48
6.5 a-b	Tungsten surface, (a) before post-deposition oxidation, (b) after oxidation	52
6.5 c-d	Same surface, (c) and (d) after oxidation	53
6.5 e-f	Same surface, (e) and (f) after oxidation	54
6.5 g-h	Same surface, (g) and (h) after oxidation	55
6.5 i-j	Same surface, (i) and (j) after oxidation	56

LIST OF TABLES

Table	Description	Page
5.1	Formula for cyanide zinc deposition	29
5.2	Median cathodic current	30

CHAPTER 1

INTRODUCTION

The field ion microscope is an ideal tool for direct viewing of the atomic structure of a solid surface because of its ability to resolve individual atoms existing at the surface of a solid specimen.

One of the recent applications of the field ion microscope has been for adsorption studies, for example: gases on metals and metals on metals, because of the vital importance of understanding adsorption phenomena. The field ion microscope is very suitable for studying these adsorption phenomena. It permits the direct observation of the diffusion of adsorbed atoms, the crystallization of adatoms directly, and also to estimate the binding forces of these adatoms to the substrate.

At the present time, a quantitative theory for metallic adsorption from field ion microscope studies is not yet available for chemisorption of diatomic gases. Several gaseous adsorption studies with investigations of corrosion due to the reactive gases have been reported[1-8]. However the qualitative results from the field ion microscope studies are still in doubt due to the uncertainties of image interpretation.

The deposition techniques for metallic thin films may be broadly classified under three headings: thermal evaporation (physical vapor deposition), cathode sputtering, and chemical deposition[9].

Several observations of thermal depositions on the field ion microscope tip have been reported: Au[10], Cu[11-13], Ir[14], Ni[13,15], Pt[16,17],

and W[18,19] on W, Ir on Mo[20], Pt on Ir[21], and Pd, Pt, Rh and Ir on either Ir or Rh[22].

The crystallization of adatoms deposited by electroplating - Pt and Cu on either W or Ir[23] - and cold welding - Au and Pt on either Ir or Pt[24] - have also been studied. Recently deposition of foreign atoms by making contacts between the tip and a liquid metal - Ga on W[25,26] and Ga on Mo[27] - have been reported. Only electrodeposition has been performed outside the field ion microscope system, all other thin film deposition having been done inside the field ion microscope.

The subject of this thesis at the initial stage was to obtain and survey strongly-bound and uniformly deposited thin zinc and zinc-oxide films on field ion microscope tungsten tip specimens. For this purpose electrodeposition of zinc and post-deposition oxidation of zinc thin films was attempted outside the field ion microscope. Unfortunately it was impossible to observe the images of the thin film surfaces because of weak binding between the films and the substrate. During almost every experiment the corrosion of tungsten tip specimen by adsorbed reactive gases was observed.

As a result of obtaining corrosion phenomena, the main interests in this thesis were focussed on the adsorbate - substrate interactions.

Zinc and zinc oxide films were investigated because of their importance application in laser and piezoelectric studies. Especially, zinc-oxide films are used for optical components (multi-layer dielectric mirrors) in gas laser systems, because of their high refractive index characteristics. For high peak power gas lasers, the most serious limitation at present is the degradation of optical

components, because these optical components are subjected to both high field stress and bombardment of ionized gases.

The investigation of zinc-oxide thin films by the field ion microscope gives information about the atomic structure of these thin films under high field stress. Also, the ion bombardment of thin films in the field ion microscope - while high fields are on - will duplicate the dielectric laser mirror action.

An unbakeable all glass high vacuum field ion microscope was used for these studies because of easy tip replacement. Also tungsten was used as a substrate because of its well - known crystallographic structure.

CHAPTER 2

PRINCIPLES OF FIELD ION MICROSCOPY

The principle of the field ion microscope was reported in 1951 by E.W. Müller[28]. Direct observation of the atomic structure of a solid surface is possible with the field ion microscope because of its high magnification and resolution (Figure 2.1). This chapter illustrates the features of the field ion microscope. The field and the stress on the field ion microscope tip are also described because of their important effect on the image formation. Detailed descriptions of the theory and application of the field ion microscope can be found in several books[29-32].

2.1 Basic principle

The microscope in its simplest form consists of the metallic specimen shaped to a finely pointed needle tip with a fluorescent screen opposite this tip (Figure 2.2). The field ion microscope operates with a small amount of pure inert gas, usually helium at pressure $1 \sim 3 \times 10^{-3}$ torr, in the chamber and with a high positive potential applied to the metallic tip. Two quite basic technical features are: (i) the provision of cooling the tip by thermal conduction through its potential leads from a cold finger filled with a cryogenic liquid, (ii) a flat fluorescent screen. A heat shield around the tip, usually at screen potential, simultaneously precools the image gas to increase the intensity and serves as a means of restricting the volume containing the electric field.

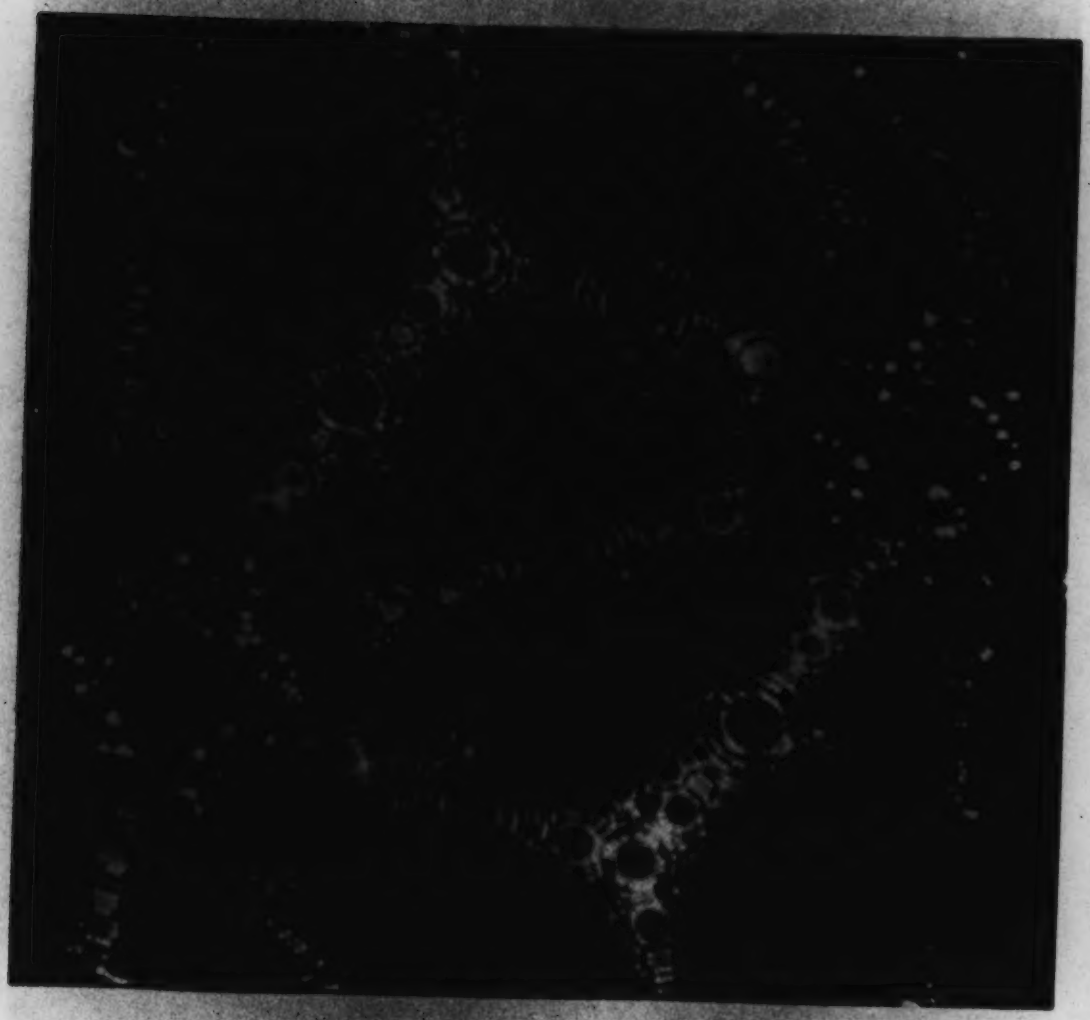

Figure 2.1 Field ion micrograph of a tungsten tip approximately 500 Å radius, image gas helium of pressure 3×10^{-3} torr, tip voltage 14.3 KV

If the tip specimen has a sufficiently small radius (below 1000 Å), the positive potential of a few kilovolts applied to the tip produces a field of the order of magnitude of a few hundred MV/cm, and ionizes the image gas in this region. The image gas pressure is low enough to provide a sufficient free path to let the ions travel to the screen without disturbing collisions. The image information is then carried from the tip surface to the screen by radially projected positive ions accelerated by the extremely high field normal to the generally hemispherical tip surface. Each white spot on the screen excited by positive ions corresponds to individual atoms on the tip surface.

The magnification is approximately equal to the ratio of the tip-screen distance to the tip radius. With a tip-screen distance of 10 cm and a tip radius of 1000 Å an image is magnified by one million times, and the resolution is often between 2 and 3 Å.

2.2 Field ionization

Field ionization is considered to be the tunnelling effect of electrons from image gas atoms into the tip. When the high electrostatic field is acting on the specimen, neutral gas atoms or molecules arrive at the specimen surface at a much greater rate than would be expected from simple kinetic theory, because of the polarization of gas molecules induced by the applied field. After striking the specimen surface, a gas atom rebounds. Provided sufficient kinetic energy has been lost to the lattice of the tip, the polarized gas atom or molecule is unable to escape from

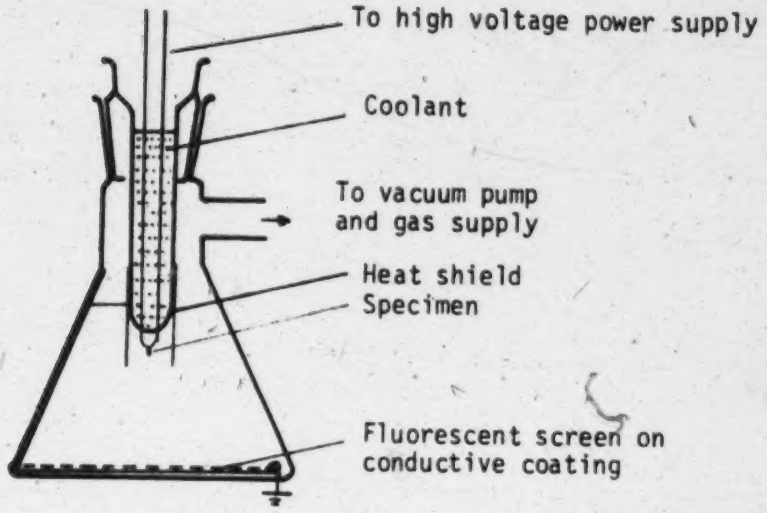

Figure 2.2

Schematic diagram of a field ion microscope

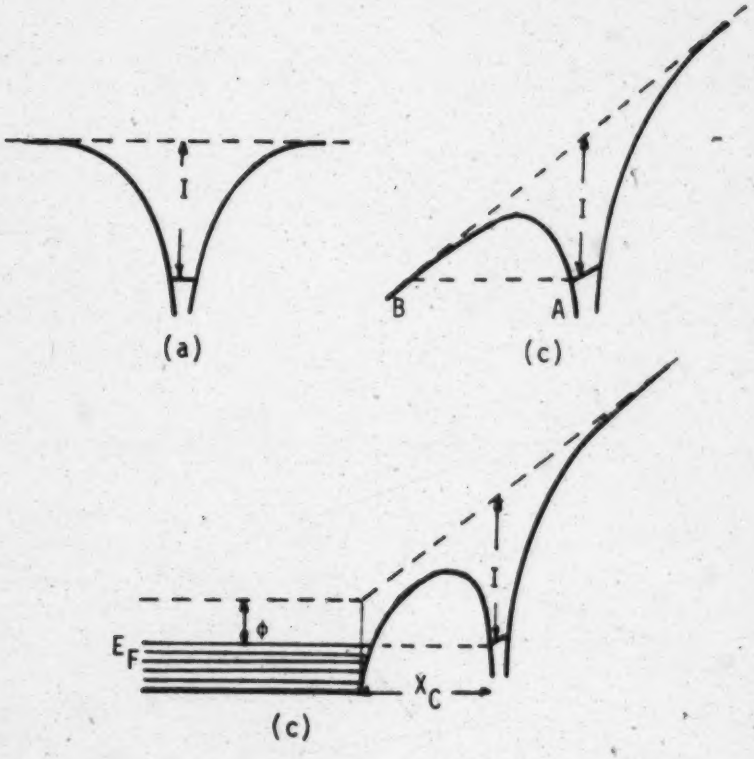

Figure 2.3

Potential diagrams for an electron in field ionization

the dipole attraction of the tip. It executes a series of jumps of decreasing amplitude, shedding energy to the lattice at each impact, and remaining for increasing times in the region of high ionization probability near the surface. When sufficiently accommodated to the specimen temperature, gas atoms or molecules lose an electron to the tip by tunnelling. Ionization will not occur at less than a certain critical distance from the surface.

The process of an electron tunnelling is considered with reference to the potential diagram shown in Figure 2.3. Figure 2.3 (a) shows the potential of an outer electron of an atom before the external field is applied: the electron lies at a potential I below the energy zero. In Figure 2.3 (b) a field has been applied to the atom and ionization can occur by the electron tunnelling along a path such as AB through the potential barrier. The tunnelling probability is increased for the atom near a conductor as illustrated in Figure 2.3 (c) where the height of the potential barrier is reduced, although the field remains the same. However, if the gas atom comes closer than the critical distance, X_c, tunnelling is unlikely to occur because the energy of the electron in the gas atom will be below the Fermi energy of the metal and there is very low density of vacant energy levels available for the tunnelling electron.

The quantitative description of field ionization also can be written for the WKB approximation[59]. The probability of tunnelling through a potential barrier of the kind indicated in Figure 2.3 (c) can

be written as;

$$P = \left\{ \frac{2m_e}{h^2} (E-V(X)) \right\}^{-1/2} \exp - \left(\frac{8m}{h^2} \right)^{1/2} \int_{X_2}^{X_1} [V(X)-E]^{1/2} dX \qquad (2.1)$$

where m_e is the electron mass, E its total energy, V(X) the potential of the tunnelling electron at a distance X from the surface, and the limits of integration refer to the barrier width. For V(X) Müller and Bahadur[33] give the following expression;

$$V(X) = \frac{-e^2}{|X_n - X|} + F_e X - \frac{e^2}{4X} + \frac{e^2}{X_n - X} \qquad (2.2)$$

where the first term is the Coulomb attraction by the ion taken to be at a distance X_n from the surface, the second term is the potential due to the applied field, and the last two terms are the attraction and repulsion at the electron and ion images respectively.

The critical distance for field ionization, X_c, can be calculated to a good approximation by assuming that it is the separation between a gas atom and a surface at which the electron energy coincides with the Fermi energy. This condition may be written after making an energy balance[34];

$$F_e X_c = I - \phi - \frac{e^2}{4X_c} + \frac{1}{2} (\alpha_A - \alpha_J) F^2 \qquad (2.3)$$

where I is the ionization potential of the gas atom, $-e^2/4X_c$ is the

potential due to the ion and its image, and the last term is the difference between polarization potential energy of the gas atom and the resultant ion. Neglecting the last two terms, which are smaller than the first two, gives the following expression for X_c:

$$X_c = \frac{I - \phi}{F_e} \tag{2.4}$$

For Helium imaging gas and a tungsten tip, substitute I = 24.5eV, ϕ = 4.5eV and F_e = 450 MV/cm (a field strength), X_c is about 4.5Å.

2.3 Field evaporation

The preparation of a clean and smooth specimen surface takes place in two stages. A specimen wire is electropolished to a fine pencil-like end form and annealed inside the field ion microscope. The final smooth of the specimen surface is achieved by the field evaporation process. If the applied field is increased to a sufficiently high value, metal atoms themselves can be evaporated from the surface lattice sites, and an atomically smooth surface, crystallographically as perfect as the bulk material can be obtained. Field enhancement over protruding surface atoms reduces the activation energy for field evaporation in these regions, so that protruding atoms at the surface of a tip specimen are evaporated preferentially. If the field evaporation is well controlled, removing atom-layer by atom-layer, the internal structure of the specimen can be explored. Despite its fundamental importance, the field evaporation process is not well understood. Field evaporation

has been treated as a desorption phenomena, and the evaporation field F_E is given as[29];

$$F_E = \frac{1}{n^3 e^3}\left[\Lambda + I_n - n\phi - kT \ln\left(\frac{\nu}{ke}\right)\right]^2 \qquad (2.5)$$

where ne is a single or multiple electric charge of the ion (n = 1 or 2), Λ sublimation energy of the metal atom, In ≡ total ionization energy, ϕ ≡ work function of the considered crystal plane, ν ≡ time required for evaporation, and ke ≡ evaporation rate of the surface.

A quantum mechanical treatment of field evaporation by considering the transition from the atomic to the ionic state was also attempted[35]. Field evaporation was treated in terms of potential energy diagrams of the metal-adsorbate system. In field evaporation the adsorbate is the surface atom itself.

2.4 The field and the stress

In the field ion microscope the specimen is subjected to very high electric fields, with consequent stresses, in order to ionize the image gas. The mechanical stress, σ, exerted on the surface by a field, Fo, will be:

$$\sigma = \frac{F^2}{8\pi} \qquad (2.6)$$

The field varies as:

$$F = Fo\left(\frac{R}{r}\right)^2 \qquad (2.7)$$

where R is the specimen radius and r is some distance such that r > R. The form of an emitter tip can be idealised as a spherical cap section, of small radius, at the end of a conical shank. The field at every point, for a given applied voltage, is proportional to the curvature and is therefore high but not strictly uniform all over the nearly spherical cap, decreasing rapidly to a low field where the cap merges with the shank. Figure 2.4 shows the field distribution for a tip of 300 Å radius, on a uniformly tapered shank, as calculated by Smith and Smith[36]. Also Figure 2.5 shows the stress distribution for a tip of 300 Å radius[36]. For tungsten imaged with helium gas the stress amounts to about 10^{11} dyne/cm^2.

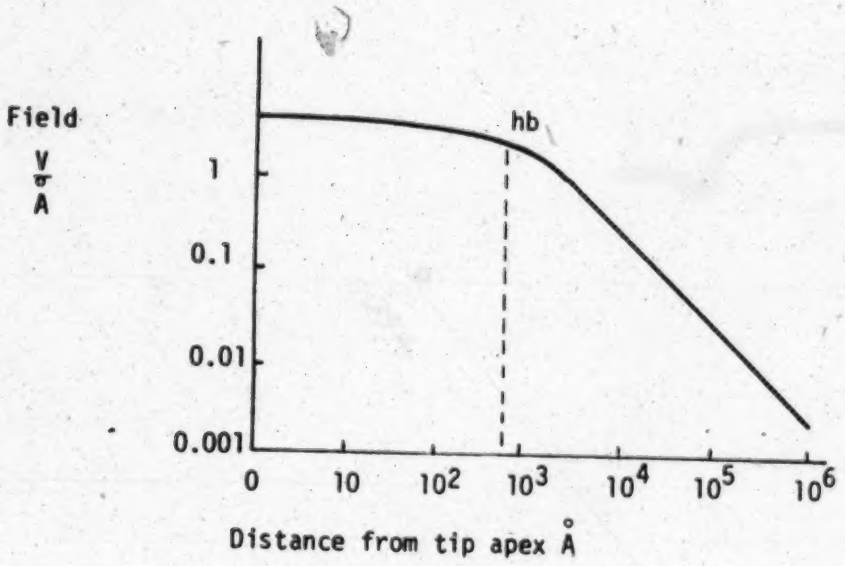

Figure 2.4

The variation of the electric field with the distance from the tip apex, for a typical specimen of radius 300Å

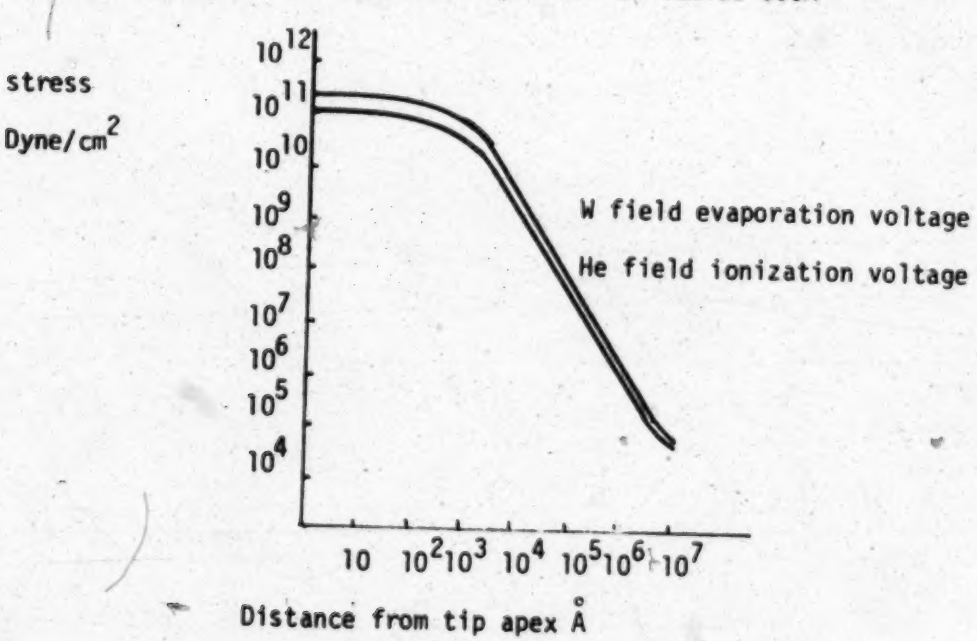

Figure 2.5

The variation of stress with the distance from the tip apex for different tip voltages, tip radius 300Å

CHAPTER 3

FIELD CORROSION

It has been recognised that, in the presence of certain reactive gases such as water vapour, oxygen and nitrogen, a field ion microscope tip may undergo continuous destruction during the imaging process. Müller has referred to the effect as "reactive gas etching"[31] and Cranstoun and Anderson use the term "field corrosion"[8].

The reactive gases reach the tip in the low field region at the circumference of the cap and at the shank, from where they migrate toward the tip apex with part of the activation energy supplied by the impact of polarized gas molecules. Etching of the shank causes the tip shape to change and thereby to increase, at constant applied voltage, the field at the tip apex. This region will then field evaporate even without being reached by the reactive gas. These corrosion effects occur frequently in insufficiently evacuated, non-bakable microscope chambers, particularly when only liquid nitrogen is available as a coolant.

3.1 The mechanism of field corrosion

There is no quantitative theory of field corrosion; its mechanism and the conditions under which it occurs are not fully understood. Several distinct factors are involved, i.e.:

(i) the supply of reactant to the high field region of the tip surface;

(ii) the effect of the high field on some reaction rate controlling factors;

(iii) the alternative final steps of desorption from, or rearrangement of, the tip surface.

It is generally considered that an emitter surface is protected by a field barrier from attack by reactive gas molecules under the conditions used for helium ion imaging because of the high imaging field. Because of the presence of this high field, reactive gas molecules are ionized in space and repelled without opportunity to interact with the tip surface. The occurrence of field corrosion therefore depends on a continuous supply of reactant below the field barrier, i.e., by migration across the surface in a adsorption layer. The field barrier effectively parts from the surface at some point hb shown in Figure 2.4, and only that part of the surface above hb is protected; the rest of the surface can chemisorb, and be continuously replenished by incident gas molecules.

The field corrosion process may then depend on the field over the spherical cap in the following manner[8].

(i) $F \geq F_{BIV}$ (F_{BIV} : Helium best imaging voltage)

It is established that strongly bound adsorbate atoms (oxygen) are evaporated from a metal surface at a field well below F_{BIV}, and that they may be field desorbed either as such - from sites on smooth planes - or may abstract metal atoms from crystallographically rather specific sites on the surface, including the edges of smooth planes, and be

desorbed as oxide molecule ions. Migrations over the surface down the chemical potential gradient - up the field gradient - brings an adsorbate at some point into a field where $F_e \leq F \leq F_{BIV}$; F_e is the evaporation field for oxide molecule ions from a particular kind of site. This will occur in some annular region around the edge of the imaged part of the tip, which will accordingly undergo continuous erosion by field evaporation, at a rate determined by the field promoted migration. The result is to decrease the local tip radius, raising the field and further promoting reaction. The attack may be highly specified to certain crystallographic planes.

(ii) $F < F_{BIV}$

At fields well below helium best image voltage, tip surface area where field desorption of adsorbed atoms or molecule ions occurs may be encountered within the imaging area. In these circumstances there will be a continuous migration of adsorbed atoms or molecules from the shank to balance the consumption by desorption and reaction in the high field region, and continuous field corrosion is observed on the tip surface.

CHAPTER 4

GROWTH AND STRUCTURE OF ELECTRODEPOSITS

The fundamental law of electrolysis was first found by Faraday in 1833. According to the law of electrolysis, the weight of the material deposited is proportional to the amount of electricity passed. The metallic ions in the electrolyte migrate toward the cathode under the influence of the applied electric field, which can be very high between the cathode surface and the ions in the double layer. According to Conway and Bockris[30,38], the cation crosses the double layer, loses part of its water of hydration, and then becomes adsorbed on the metal surface as an adion. The adion diffuses over the surface, loses the rest of its water of hydration, and is finally incorporated as an ion into the metal lattice.

4.1 Nucleation and growth of electrodeposits

At first the growth of the crystal from the vapor can be discussed briefly because many of the concepts are directly transferrable to the case of electrodeposition.

The surface of a perfect crystal may be classified as composed of either close-packed (low index) surfaces or vicinal (high-index) surfaces. In this classification a high-index plane is always stepped on an atomic scale whereas a low-index plane is generally considered as smooth. The steps on the high-index surfaces are segments of close-packed planes and these steps will always have a high concentration of

kink sites (Fig. 4.1). For example, typical micrographs of field ion microscope tips show that certain orientations such as (111) and (100) in face cubic crystal lattices and (110) in body cubic crystal lattices are atomically flat terraces. Vicinal orientations are found to be composed of monoatomic steps separated by segments of terraces, and some steps are atomically straight and close-packed while others are kinked or jogged.

If atoms are added to a vicinal surface from a supersaturated vapor, three major steps are involved in its growth[39] : (a) adsorption of atoms on the surface, (b) surface diffusion of the atom to a step, and (c) diffusion along the steps to a kink site. The steps on the surface will then advance by the addition of atoms at the kink sites until the steps grow out of the crystal, leaving only low-index surfaces.

It is obvious that certain major differences exist between the growth of crystals on a surface by vapor deposition and the growth by electrodeposition. The major differences would arise from the presence of an environment about the crystal surface consisting of a water solution containing various anions and cations, the presence of a high electrical field and the lower temperature in electrodeposition. Many vapor depositions are carried out in a high vacuum and at relatively high temperatures.

A metal surface in an aqueous solution will have adsorbed layers which decrease the surface energy of the metal and make the surface diffusion of the deposit ions or atoms considerably more difficult.

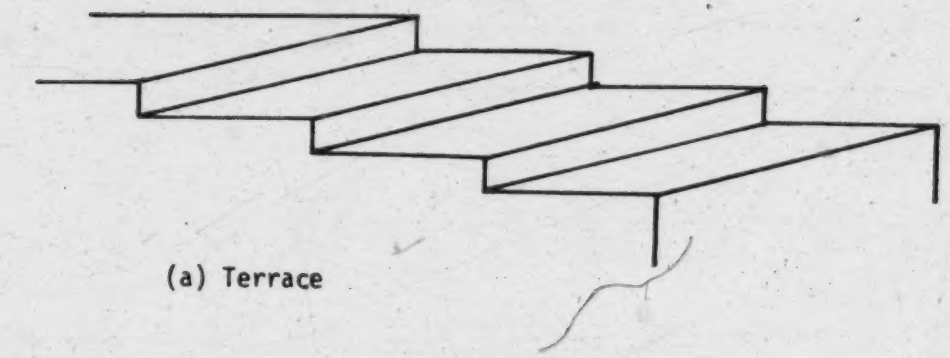

(a) Terrace

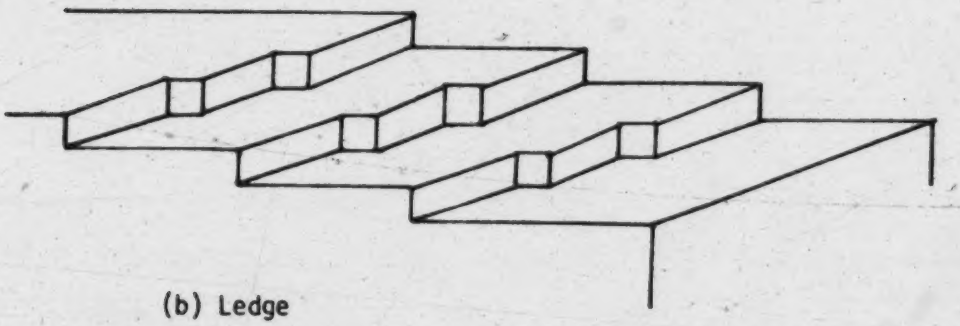

(b) Ledge

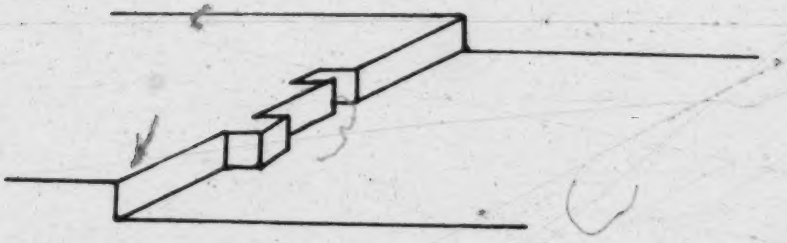

(c) Kink

Figure 4.1

Simple Terrace-Ledge-Kink model

On the other hand, if the adsorbed cations are hydrated, their bounding to the metal surface would be weakened and the activation energy needed for surface diffusion would be expected to be less than that for unhydrated atoms on the surface[40].

It is known that a cation in aqueous solution is closely bound by a sheath of water molecules, i.e., it is a hydrated ion. Before such an ion can be made a part of the crystal lattice, it must first cross the double layer and then lose its sheath of water molecules. In the first step the solvated cation crosses the double layer, loses part of its water of hydration, and the cation becomes adsorbed on the metal surface as an adion. Theoretical considerations[37,38] indicate that the ion transfer takes place at planar portions of the metal surface, rather than at edges or kink sites. An unfavorably high activation energy would be required at edges or kink sites because of the extra energy needed to remove most or all of the water of hydration about an ion in one step.

The second step involves the surface diffusion of the partially hydrated adion until it reaches a edge on the crystal surfaces, at which site it loses additional water of hydration. The adion finally loses the last of its water of hydration and becomes incorporated as an ion into the metal lattice after surface diffusion along the edge to a kink site, or the adion becomes increasingly co-ordinated by other ions which arrive subsequently, stays at the edge, and becomes incorporated as an ion into the metal lattice. Figure 4.2 shows alternative and consecutive steps in lattice building: (a) direct transfer of an ion I to a planar

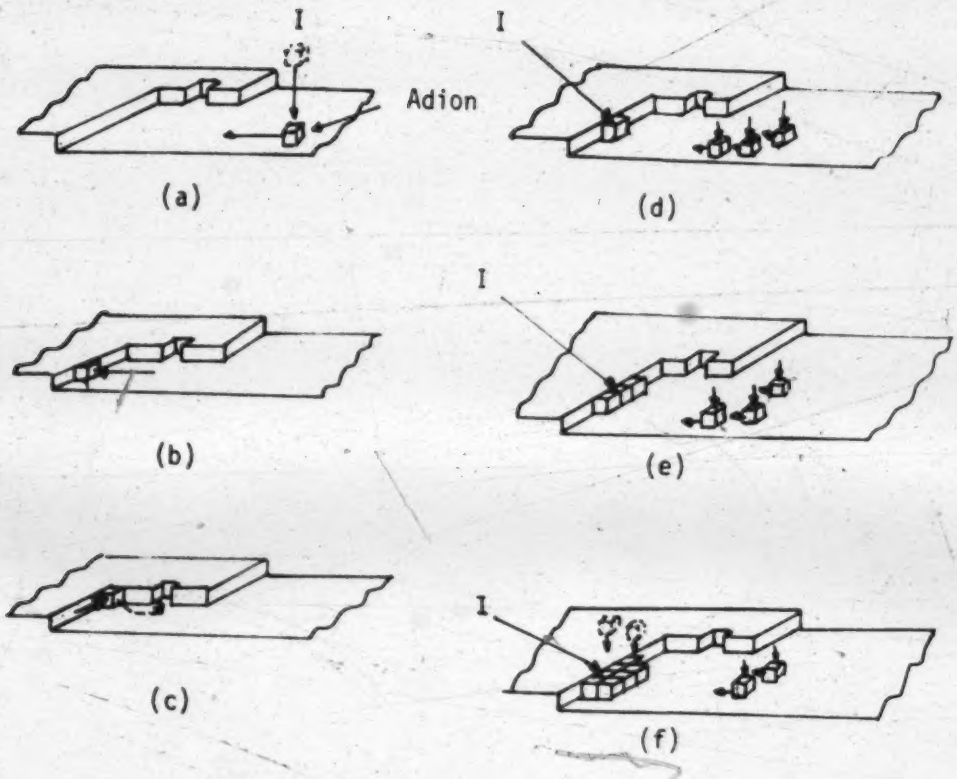

Figure 4.2

Alternative and consecutive steps in lattice building

portion of surface, (b) and (c) show surface and edge diffusion of adion, (d) shows arrival of other adions, which by surface diffusion build around the adion I at the edge, and (e) and (f) show incorporation of I into the lattice by arrival of other adions migrating across the surface or transferred from the solution.

The deposition rate is proportional to the electrolysis time and the current density, and may be varied over a wide range from about an angstrom to several microns per second. The structure of the deposit depends sensitively on the rate of deposition and the characteristics of the electrolye, and may vary from a highly disordered to a well-oriented single crystal.

4.2 Formation and lattice structure of zinc and zinc-oxide films

Zinc is one of the most active metals. Reaction with atmospheric oxygen at low or medium humidity causes the freshly prepared zinc surface to become covered with a pseudoamorphic film of zinc-oxide, which after a few hours is transformed into an ordinary crystalline film whose growth is linear[41].

Thin films of zinc are usually prepared by evaporation in a high vacuum or electrodeposition. The thin films of zinc-oxide are obtained indirectly by post-deposition oxidation of zinc films, or directly by reactive sputtering in an oxygen-argon inert gas[42-45]. Post-deposition oxidation is usually carried out by heating the thin film in air or oxygen to the range between 600°K and 900°K[46].

Zinc films are electrodeposited from acid or alkaline solutions. In acid solutions zinc is present in the form of simple hydrated ions which are discharged at the cathode at a low polarization, while in alkaline solutions zinc is present in the form of complex ions whose discharge is accompanied by a considerable cathodic polarization.

Due to the low cathode polarization the deposits obtained from acid solutions are more coarse-grained than those plated from alkaline solutions. Intricately shaped items are mostly plated in alkaline cyanide solutions which produce a fine-grained deposit. Cyanide zinc-plating solutions differ from cyanide solutions used for depositing other metals in that they contain two kinds of complex ions: $Zn(CN)_4$ and ZnO_2[47]. The electrolyte should contain free NaCN and NaOH in excess of the amounts needed for the formation of the soluble complexes in order to render the solution stable and then permit the normal anodic and cathodic processes to take place. Thus, alkaline cyanide zinc deposition solutions contain at least four components: $Na_2Zn(CN)_4$, Na_2ZnO_2, NaCN and NaOH[48]. The exact ratio of sodium zincate to sodium zinc cyanide complex is impossible to determine. The equilibrium is affected by the relative concentration of uncombined sodium cyanide and sodium hydroxide in the bath. Zinc ions are available in the solution from both sodium zincate and the complex sodium zinc cyanide. The following equations show the probable ionization[47]:

(1) $Na_2Zn(CN)_4 = 2\ Na^{++} + Zn(CN)_4^{--}$

$Zn(CN)_4 = Zn^{++} + 4\ (CN)^-$

(2) $Na_2Zn(CN)_4 + 4NaOH = Na_2ZnO_2 + 4NaCN + 2\ H_2O$

$Na_2ZnO_2 = 2\ Na^{++} + ZnO_2^{--}$

$ZnO_2^{--} + 2H_2O = Zn^{++} + 4\ (OH)^-$

Zinc crystal has the hexagonal close-packed structure with $A_o = 2.6648\mathring{A}$ and $C_o = 4.9467\mathring{A}$ [49] and belongs to the low-melting point soft metals (melting point = 419°C).

In many of its properties zinc-oxide stands between the heteropolar alkali halides and the homopolar semiconductor of Group IV[46]. The crystal structure of zinc-oxide is hexagonal close-packed of wurtzite type with two significant characteristics. The first is the large extra volume with large void ($0.94\mathring{A}$), and the second is the regular alternating layer of zinc and oxygen in the direction of the c-axis. Crystal data is given as: $A_o = 3.2495\mathring{A}$ and $C_o = 5.2069\mathring{A}$[49]. An alternate form of zinc-oxide thin film with a face centred cubic crystal lattice was identified by Bragg and Darbyshine[50].

CHAPTER 5

EXPERIMENT

Electrodeposition and its post-deposition oxidation have been achieved outside the field ion microscope. Easy tip replacement was required; therefore; an unbakable, all glass field ion microscope has been used in all experiments. In order to observe rapid image changes at low applied voltage, an external image intensifier was used.

The electrical equipment used in this experiment has been described in great detail in another article.[51]

5.1 The microscope chamber

Figure 5.1 shows the microscope chamber used in this experiment. The basic features are exactly the same as in Figure 2.1. A conventional rubber o-ring is used for the specimen dewar and screen plate seals. Aluminum foil is used for the heat shield. The chamber consists of pyrex glass except for the bottom part of the specimen dewar which consists of uranium glass for greater mechanical strength. Two specimen dewars of the same size are used in order to achieve quick tip replacement.

The radius of the screen plate is about 15cm. The tip to screen distance is about 5 cm.

The tip (0.004" diameter and 99.95% purity tungsten wire) is spot-welded on a hairpin shaped heat loop (0.005" diameter and 99.9% purity tungsten wire) which is also spot-welded on a potential lead.

5.2 Vacuum System

The main pumping system consists of a mercury diffusion

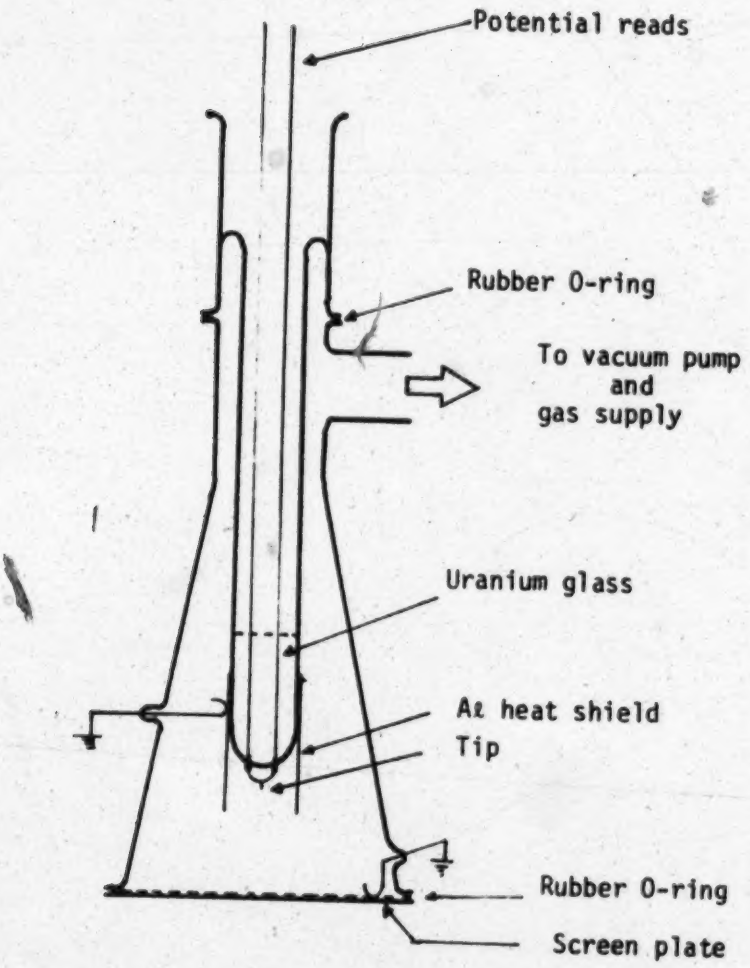

Figure 5.1

Microscope chamber

pump and an ion pump. Figure 5.2 shows the diagram of the vacuum system with the gas handling plant (GHP). A two stage rotary pump (CenCo-Hyvac 7) reduces the pressure of the system to the 10^{-3} torr range and serves to back a two stage mercury diffusion pump which is trapped by two liquid nitrogen cold traps. The system is pumped to high vacuum by the mercury diffusion pump and an ion pump (Ultek, 9 liters/sec).

The background pressure of 2×10^{-7} torr is usually achieved after 24 hours of pumping. By filling the specimen dewar with liquid nitrogen, the system achieves a pressure of about 5×10^{-8} torr. This pressure is measured by a cold cathode ionization gauge (H.S. Martin and Son). During image operation, a pirani gauge (Speedvac, Model 8/2) is used as the pressure monitor, because the ionization gauge is turned off to avoid excess light due to discharge of the gauge.

5.3 Gas handling plant

Figure 5.2 also shows the gas handling plant (GHP) . Image gases are introduced into the microscope chamber through a variable leak valve. The GHP is pumped by a rotary pump in order to maintain the purity of the image gases. After filling the cold traps with liquid nitrogen, a background pressure of the order of 10^{-3} torr is achieved. Image gases of research grade purity (He, Ne and H_2) are supplied in 1 liter glass flasks (G_1, G_2 and G_3 in diagram). Another two flasks (G_4 and G_5) are used as reservoirs of pure or mixed gas.

The pressure in the GHP is measured by a pirani gauge (Speedvac, Model 8/2). Also a mercury level manometer and a McLeod gauge (Vacustat)

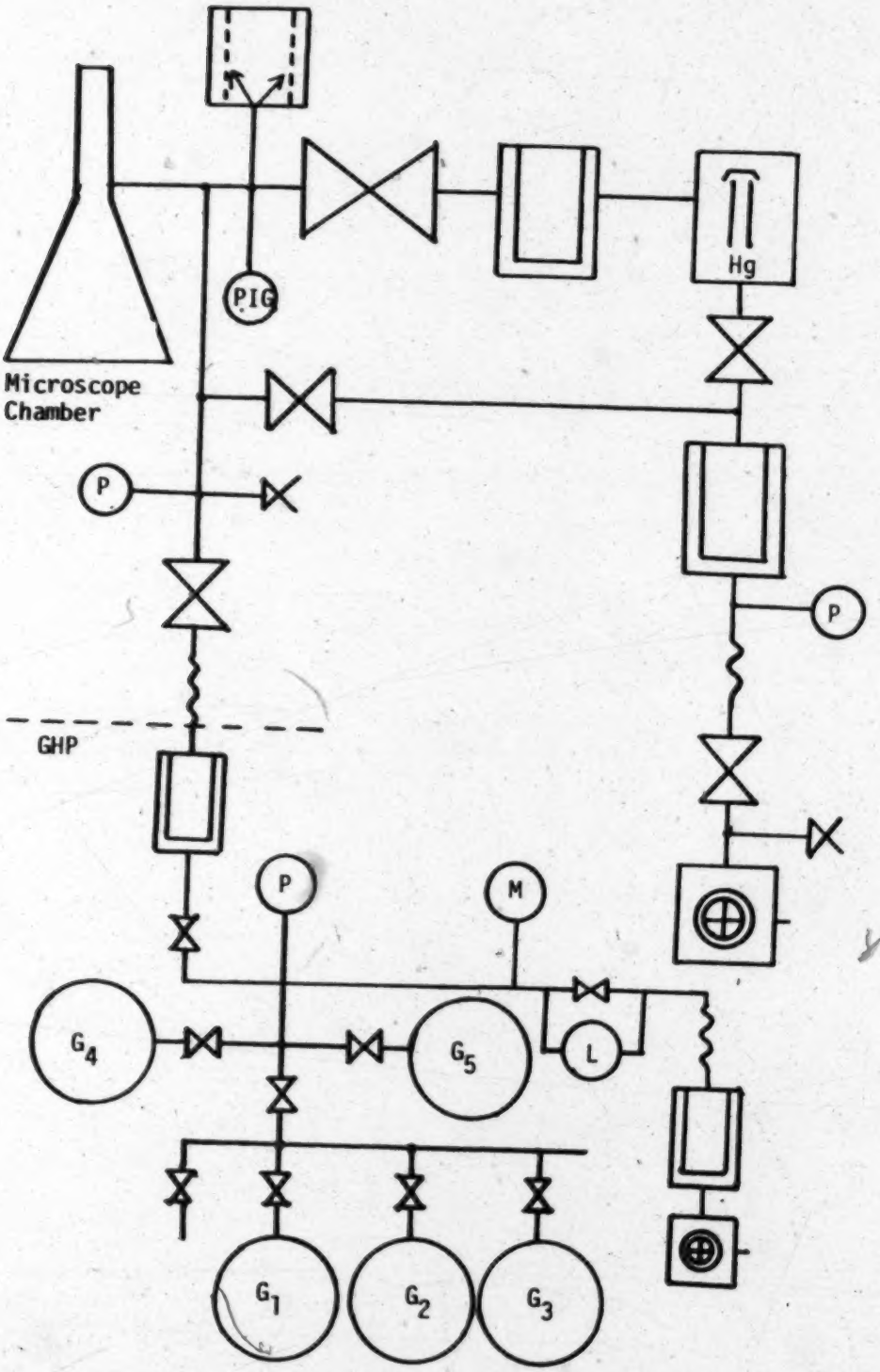

Figure 5.2

FIM System Diagram

is provided for measuring different pressure ranges when mixing the imaging gas medium.

5.4 Specimen preparation

The tip is electropolished in the usual manner[51] and then field evaporated to achieve a clean and atomically smooth surface inside the field ion microscope before electrodeposition. By controlling the field evaporation rate, a tip radius of about 500Å is always obtained before electrodeposition, applying about 13KV of helium best image voltage. After obtaining the field evaporation end form, the tip is taken out of the field ion microscope and electrodeposition and its post-deposition oxidation are carried out as soon as possible to minimise the effect of atmospheric adsorption. Usually electrodeposition has been done within ten minutes and its post-deposition oxidation within twenty minutes.

The commonly used cyanide zinc plating solution is also used for this experiment. The formulas are given as follows[47,48]:

Solution composition	gram/liter
Zinc Cyanide $Zn(CN)_2$	60
Sodium Cyanide NaCN	23
Sodium hydroxide NaOH	53
Operation conditions	
Temperature	40-50°C
Current density	1 A/cm^2-2A/cm^2
Cathode current efficiency	90-95%
Anode - high grade zinc	99.9%

Table 5.1 Formula for a cyanide zinc deposition

The tip is immersed to a depth of about 2mm into the plating solution which is at a temperature of about 45°C. The deposition times are varied from 10 - 120 seconds. Because of the extremely sharp electrode shape, it is impossible to know the exact current density at the tip apex. To determine the magnitude of current density, one must compare the surface area of the tip apex with that of the tip shank and choose the median. For example if the electrode is a 0.004" diameter and 2mm long rod, the surface area is about 6×10^{-3} cm^2; for a 500Å diameter and 2mm long rod, it is 3×10^{-6} cm^2. Therefore, the median surface area will be roughly 1×10^{-4} cm^2. Then the cathodic current which will be needed to characterize a deposit of this surface area can be easily found according to the following:

Current density	Cathodic current
0.1 A/cm^2	10μA
1 A/cm^2	100μA
10 A/cm^2	1mA

Table 5.2 Median cathodic current

After electrodeposition, the tip specimen is heated up to about 400°C in air in order to make a zinc-oxide film. This is done by applying constant electrical current to a heat loop. The approximate temperature of the tip can be obtained by measuring the resistance of the tungsten heat loop. The heat loop is a 0.005" diameter and 2cm long tungsten wire, and at 427°C resistivity of tungsten (ρ) is $16.09 \times 10^{-6} \Omega cm$[52]. therefore the resistance of the heat loop at 427°C

(R_{427}) is $R_{427} = \rho \ell/A = 0.25\Omega$. By applying a 1.8A AC current, $R_{427} = 0.25\Omega$ is obtained. However, the heat gradient in the heat loop is not uniform; the center part is considered to be much hotter than the edge. Therefore, for oxidation of the zinc film on the tip, a 1.7A AC current is used for 10 min in all experiments in order to achieve a temperature closer to 400°C.

5.5 Photography and image intensification

Since image intensities are very low in the field ion microscope, the best available photographic or image intensification equipment is required for better results.For these experiments a Miranda 35mm camera with an Auto-Minolta F 1.4 lens and an EMI 4-stage cascade external image intensifier with an Auto-Miranda F 1.9 lens has been employed. By using an external image intensifier, the resolution of the image is decreased; however, exposure time is reduced by a factor in the order of 10^3. Therefore rapid changes in the tip conditions are considered to be easily recorded. However attempts at getting well - resolved images have not been successful because of poor optical coupling.

A highly sensitive panachromatic film (Kodax Tri-X Pan) processed with a highly active developer (Diafine) is also used for experimental work.

5.6 Experimental techniques

After about 24 hours of pumping, a chamber background pressure of 2×10^{-7} torr is obtained. Then the specimen dewar is filled with liquid nitrogen. After cooling the system to the liquid nitrogen temp-

erature, the pressure falls to approximately 5×10^{-8} torr. After this pressure is obtained, the baffle valve is partially closed until a certain flow rate is established. Also the ion pump is turned off. Then the leak valve is open to a certain leak rate to maintain an equilibrium pressure of the image gas in the microscope chamber of approximately 3×10^{-3} torr for helium. The microscope chamber is continuously pumped during the imaging period. The helium image gas pressure is measured by the ionization gauge first, and during the imaging period, is monitored by the pirani gauge.

After the equilibrium condition of the helium image gas pressure is achieved, high voltage is gradually applied to the tip in order to observe the change of the surface topography on the tip.

A new tip specimen is always heated to a dull red heat for outgassing, and then field evaporated to make a clean and atomically smooth surface. The images of tip specimens after deposition and its post-deposition oxidation are taken directly without outgassing because of the low melting temperature of zinc and zinc-oxide as compared to that of tungsten.

CHAPTER 6

RESULTS AND DISCUSSIONS

In order to interprete correctly the significance of the images of electrodeposited specimens, the effects of both atmospheric adsorption and the effect of the deposition solution on the tip specimen were determined.

Experiments to determine the effects of both of these factors were carried out. A total of 40 experiments were carried out by using 10 different tip specimens. The statistical nature of the experiments are as follows:

atmospheric adsorption ... 5 experiments for 5 tips

deposition solution ... 5 experiments for 5 tips

electrodeposition ...20 experiments for 10 tips

post-deposition oxidation ... 10 experiments for 10 tips

After each experiment, the tip specimen was always outgassed and field evaporated in order to achieve an atomically clean and smooth surface for the ensuing experiments. The micrographs shown in this chapter represent typical patterns observed in each experiment.

A micrograph was taken at first before deposition. After deposition, micrographs of changing tip surface topographies were taken, from a low applied voltage to a high applied voltage, until the image of the clean tungsten crystal structure appeared.

6.1 The effect of atmospheric adsorption

After obtaining the field evaporation end form, the system was opened to air for about 20 minutes to investigate the effects of

atmospheric adsorption on the tip specimen.

With the adsorption of reactive gases in air, mainly oxygen, the perfect field evaporated surface rapidly changed. The image was observed at voltages far below the original helium best image (He BIV), indicating that the field was strongly enhanced at local protrusions, and field desorption events became evident. Brilliant image spots were seen to wander randomly across the surface before being desorbed.

Figure 6.1(a) shows the field evaporation end form at 13.2KV before opening the system to air. Figures 6.1(b) - 6.1(f) show the micrographs after atmospheric adsorption : (b) at 8.8KV, (c) 10.3KV, (d) 11KV, (e) 12KV and (f) 13.6KV.

The layers of adsorbed gases were removed by raising the applied field on the surface. The adsorbed atoms or displaced tungsten atoms were removed from metal surfaces in a particular order. The first regions of the surface to become free from adsorbed atoms were the (211) pole regions where the radius of curvature of the tip was smallest. Then the low index, higher radius of curvature regions such as (100) and (111) were cleared. Finally, the central (110) terrace regions were cleared at almost the same applied voltage as the original HeBIV. In general, the specimens did not fracture during this operation. Also the drastic changes of tip surface topography by atmospheric adsorption were not observed in this operation.

There have been many arguments of interpretation of imaging the extra spots after field desorption of adsorbates, such as shown in circles in Figure 6.1 (f). Ehrlich[1-3] studied CO and N_2 adsorbed on tungsten emitters, using He as the imaging gas, and concluded that the

Figure 6.1 (a) Clean tungsten surface taken at 13.2 KV

Figure 6.1 (b) After atmospheric adsorption taken at 8.8 KV

Figure 6.1 (c) Same surface at 10.3 KV

Figure 6.1 (d) Same surface at 11.0 KV

Figure 6.1 (e) Same surface at 12.0 KV

Figure 6.1 (f) Same surface at 13.6 KV

resulting extra spots corresponded to images of the adsorbates. On the other hand, Holscher and Sachtler[4] concluded that at the field required for imaging with He, all or most of the adsorbate had been field desorbed and the extra spots correspond to displace tungsten atoms. Müller[53] had shown earlier that oxygen was field desorbed at 4.5v/Å in the presence of He. From experiments of an atom probe FIM he concluded that field desorption removed some metal, as well as oxygen, atoms. Recently Lewis and Gomer[7] suggested two points: first, most adsorbates were field desorbed below He imaging fields; second, much of the disorder seen after field desorption of the adsorbate is the result not of adsorption but the desorption act itself.

For a tungsten surface, oxygen has the biggest accommodation coefficient among the diatomic gases[54]. The extra spots in Figure 6.1 (f) and the random spots in (110) terrace area in Figure 6.1 (d) and (e) represent therefore displaced tungsten atoms. Also the brilliant spots shown in Figure 6.1 (b) and (c) are presumably mobile clusters or oxide proto-nuclei, not strongly bound to the surface, and themselves arising from aggregation of individual molecular units detached from the metal surface. At room temperature, oxygen is weakly adsorbed and a nearly perfect surface is reattained only by desorbing several atom layers of tungsten.

6.2 The effect of deposition solution

After obtaining the field evaporation end form, the tip specimen was immersed into the deposition solution for about 2 minutes, to determine the effects of the deposition solution on the specimen.

Figure 6.2 (a) - (d) shows the typical micrographs before and after the immersion of the tip into the solution. Figure 6.2 (a) shows the clean tungsten surface at 13.0KV before the immersion. Figure 6.2 (b) - (d) show the contaminated surface with air and deposition solution : (b) was taken at 10.2KV, (c) 11.0KV, (d) 11.2KV.

The micrographs show the same pattern as shown in Figure 6.1. Namely, the brilliant image spots shown in Figure 6.2 (b) are presumably mobile clusters or oxide protonuclei, not strongly bound to the surface. The clean tungsten surface shows up in a particular order, - i.e., from the region with smaller curvature to the region with larger curvature of the tip.

In this operation the reconstruction of the tunsten surface is observed. In Figure 6.2 (b), type (i) corrosion in section 3.1 is observed around theperipheral (110) region (shown by arrows). This corrosion effect decreases the local tip radius, raising the field and further promoting the reaction. Comparing Figure 6.2 (d) with (a), the reduction of peripheral (110) plane rings is obvious. Also Figure 6.2 (d) shows the reduction of the central (110) plane rings. These are the results of corrosion induced reaction in local radius of curvature of the tip. At the end of the process, the HeBIV is reduced to about 20% of original HeBIV.

One central problem of field ion microscopy is the proper interpretation of image contrast. Structural changes and conservative rearrangements of the surface lead to a redistribution of the field, but the nature of the topographic changes cannot always be inferred directly and unambiguously from the image. A bright area (field

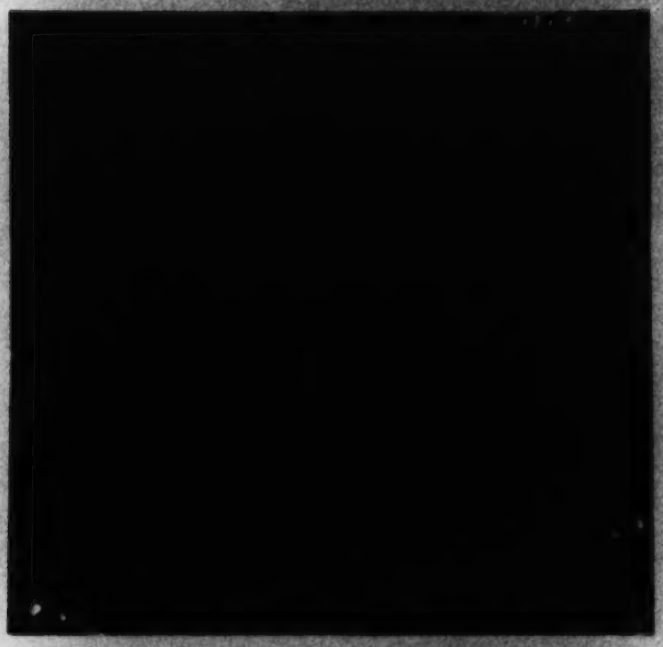

Figure 6.2 (a) Clean tungsten surface taken at 13.0 KV

Figure 6.2 (b) After immersion to solution taken at 10.2 KV

Figure 6.2 (c) Same surface at 11.0 KV

Figure 6.2 (d) Same surface at 11.2 KV

enhancement, high curvature) can be due either to deposition of material at that place, or to erosion of the surface around it. A dark area can be due either to erosion and removal of one or more surface atom layers or to deposition of material nearby, so that the built up part becomes visible at a lower voltage. Also, partial field evaporation from parts of a rearranged or perturbed surface can take place at a very low averaged field, especially from high curvature regions and in the presence of chemisorbed oxygen.

In Chapter 3 the effect of a high field on tip surface are summarised as (i) providing a continuous supply of reactant to the tip area, and (ii) accelerating the primary stages of the corrosion reaction proper, by lowering the activation energy for distorting the configuration of a surface site. Within the tip area, adsorbate species migrate up-field from site to site, and their movement at each migratory step depends on the balance between deposition field and site binding properties.

Therefore, the reason of the reduction in local radius of curvature is considered as (i) a site-selective degradation of the original surface structure, (ii) a deposition of material on specific areas, and (iii) a net loss of material by field desorption.

In operation 6.1, the reduction in the local radius of curvature due to corrosion were not observed. The changes in surface topography observed in this operation are therefore considered to be due to the strong reaction between the tungsten tip and water molecules which are adsorbed during immersion of the tip into deposition

solution.

6.3 The effect of electrodeposition

The electrodeposition of zinc was carried out for different current densities and deposition times. By using AC current, the tungsten tips become etched, and the thin zinc films were not obtained. By using DC current, the tungsten tips become grey-tarnished, showing that they are coated with zinc.

At 500μA DC, the coatings are too thick to allow an observation of the images below 30KV imaging voltage. Also at 50μA DC, it was difficult to observe the change of tip colour as electrodeposition proceeded. The best electrodeposition condition was experimentally determined to be 100μA DC for 30 seconds. For this condition, the change of tip colour was easily observed and an image could also be observed at a "normal" imaging voltage.

Figure 6.3 (a) - (f) show the typical images of the tip before and after electrodeposition at 100μA DC for 30 seconds. (a) is taken at 13.6KV before electrodeposition, (b) is at 8.1 KV after electrodeposition, (c) at 9.2KV, (d) at 10.0KV, (e) at 9.4KV and (f) at 9.8KV.

Figures 6.4 (a) - (j) were taken by using the external image intensifier for the tip, before and after electrodeposition for the same conditions as Figure 6.3 (a) - (f). Figure 6.4 (a) is taken at 10.4KV before electrodeposition, (b) is taken at 7.2KV after electrodeposition, (c) at 7.6KV, (d) at 7.7KV, (e) at 7.8KV, (f) 7.9KV, (g) at 8.0KV, (h) at 8.1KV, (i) 8.2KV and (j) at 8.3KV.

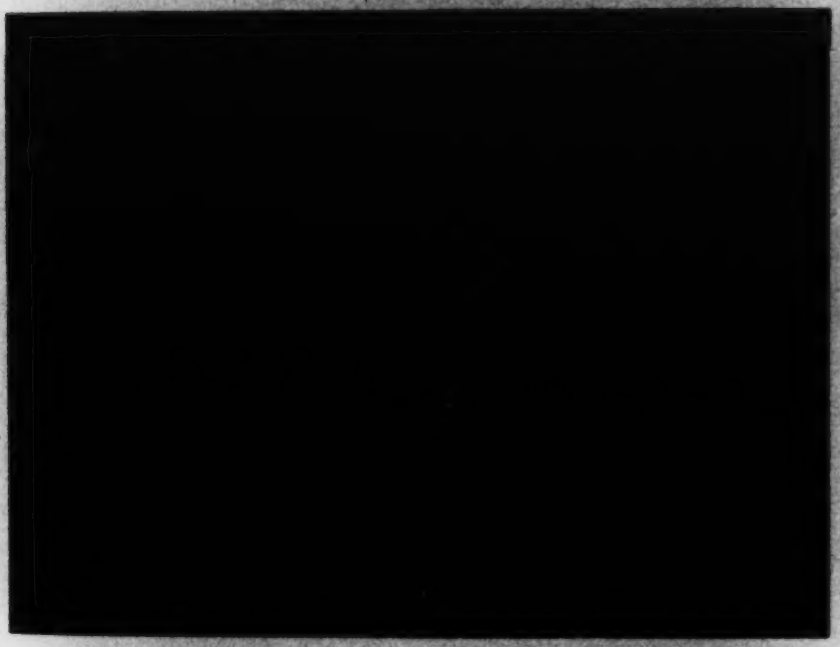

Figure 6.3 (a) Clean tngsten surface taken at 13.6 KV

Figure 6.3 (b) After electrodeposition taken at 8.1 KV

Figure 6.3 (c) Same surface at 9.2 KV

Figure 6.3 (d) Same surface at 10.0 KV

Figure 6.3 (e) Same surface at 9.4 KV

Figure 6.3 (f) Same surface at 9.8 KV

Figure 6.4 (a) Clean tungsten surface taken at 10.4 KV

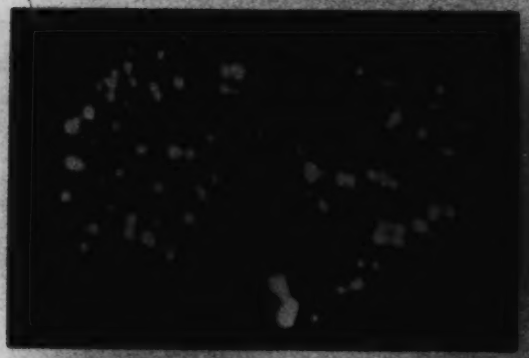

(b) After electrodeposition taken at 7.2 KV

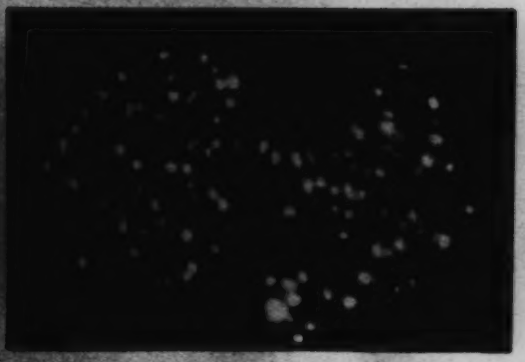

(c) Same surface at 7.6 KV

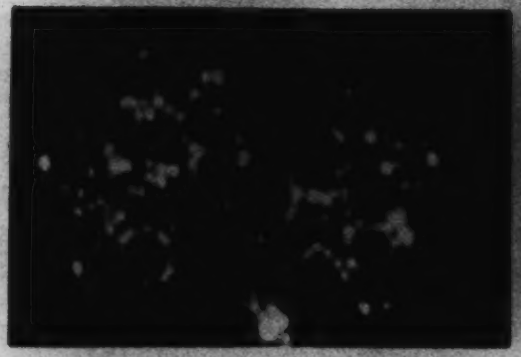

(d) Same surface at 7.7 KV

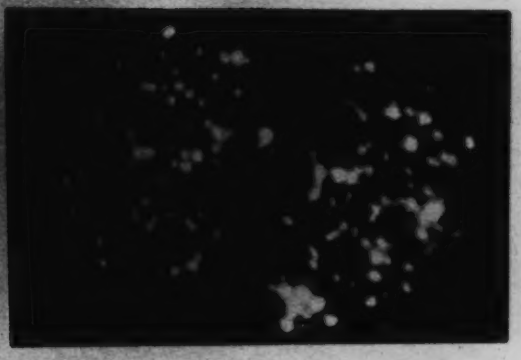

(e) Same surface at 7.8 KV

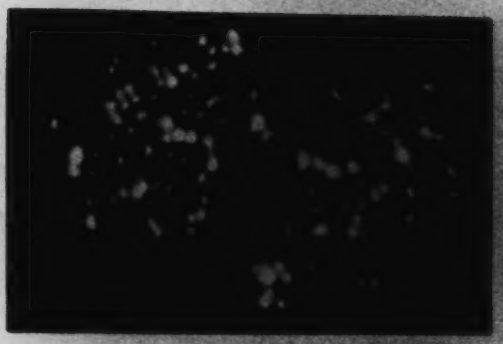

(f) Same surface at 7.9 KV

(g) Same surface at 8.0 KV

(h) Same surface at 8.1 KV

(i) Same surface at 8.2 KV

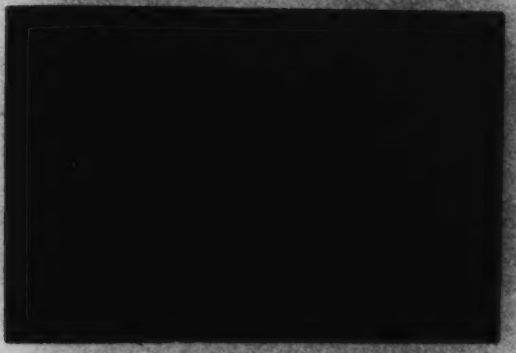

(j) Same surface at 8.3 KV

By using the external image intensifier, the detail change of surface topography could be recorded, but the resolution is bad compared with Figure 6.3. Moreover, it was extremely difficult to interpret image contrast because of the sensitivity of the external image intensifier.

In this operation, the extensive and continuous changes in surface topography were observed through each series of micrographs. After careful interpretation of the micrographs, the images were determined as being corrosion processes of the tungsten tip for the following reasons;

(1) images were taken far below the original HeBIV.

(2) the reduction in local radius of curvature of the tip was observed.

(3) the streaks in the centra (110) region were a common phenomena due to the interaction of the tungsten tip with reactive gases, mainly water molecules[55].

(4) the images show the body centred cubic crystal lattice structure which tungsten exhibits.

The thin zinc films were hence considered to be weakly bonded to the tungsten substrate and could be easily ruptured under the helium imaging field.

The corrosion patterns shown in Figure 6.3 and Figure 6.4 are representative of type (ii) corrosion in section 3.1. Namely, at a field well below the original HeBIV. (in Figure 6.3 (b), 67% of the original HeB IV). (in Figure 6.4 (b), 69% of the original He B IV), the field at which field desorption of adsorbed atoms or molecules occurs is encountered within the imaging area. In these circumstances there

will be a continuous migration of adsorbed atoms or molecules from the shank to balance the consumption by adsorption and reaction in the high field region, and for this condition continuous field corrosion was observed. The images of continuous field corrosion were observed in the central (110) region in Figure 6.3 (b) through (e) and in Figure 6.4 (b) through (i). In Figure 6.3 (c) and 6.4 (e), the (110) region appears to be doubled from the (111) pole area to the (11T) pole area. After further field evaporation, the central streak through (111) to (11T) appears in Figure 6.3 (d) and 6.4 (h). This "doubling" or streak on the (110) terrace zone is considered to be the corrosion front. The (110) face is the closest packed in a body centred cubic crystal lattice, but is surrounded by atomically rough surfaces in all directions except in cases such as (110)-(211). These latter consist entirely of terraces of (110) orientation. Also the surface is atomically much rougher near (111) than (100). It is reasonable to assume that crystallographically selective erosion occurs at most atomically rough surfaces near (111) and thus creates the corrosion front from (111) through (110) to (11T).

After further field evaporation, a clean tungsten surface (Figure 6.3 (f) and 6.4 (j)) appeared at 72% ~ 80% of original HeBIV. The reduction in local radius of curvature was significantly large, and the tip (about 150 Å in radius) was almost spike-like in shape. This apparently resulted from a catastrophic symmetrical corrosion of the tip at the boundary of the high field region. The corroded region of the tip surface was fully imaged at a He BIV lower than that of the original surface. The "doubling" or streak on the (110) terrace zone

is thus explained by erosion at and transport from these (110) terrace sites, some of the eroded atoms being built up at the corrosion edge in competition with field evaporation. Further attack on the already corroded surface segments occurred by the advance of another corrosion edge. The mechanical stresses at these fields were too low to cause catastrophic slip and fracture. As a result, the corrosion process could proceed symmetrically from all sites to give the pointed end form. The main reactant in this corrosion process is considered to be oxygen and water molecules which were trapped as a hydrate during electrodeposition, because the streak around the (110) region was often found when water molecules existed inside the microscope chamber[55].

6.4 The effect of post-deposition oxidation

After electrodeposition of zinc on the tip specimen at 100μA DC for 30 seconds, the specimen was oxidized in air while an AC current of 1.7A was applied for 10 minutes through the heat loop.

Figures 6.5 (a) - (j) show the effect of post-deposition oxidation : (a) was taken before any treatment at 13.5KV, (b) after post-deposition oxidation at 7.4KV, (c) at 8.4KV, (d) at 9.0KV, (e) at 9.7KV, (f) at 10.2KV, (g) at 10.4KV, (h) at 12KV, (i) at 13.8KV, and (j) at 16KV.

In this operation it is also considered that the images were not those of the zinc-oxide thin film, but the images of the corrosion of the tungsten substrate for the same reasons mentioned in section 6.3. The pattern of corrosion shown in Figure 6.5 (b) to (g) is representative of type (ii) in section 3.2. Another pattern of corrosion (type i) in

Figure 6.5 (a) Clean tungsten surface taken at 13.5 KV

Figure 6.5 (b) After post-deposition oxidation taken at 7.4 KV

Figure 6.5 (c) Same surface at 8.4 KV

Figure 6.5 (d) Same surface at 9.0 KV

Figure 6.5 (e) Same surface at 9.7 KV

Figure 6.5 (f) Same surface at 10.2 KV

Figure 6.5 (g) Same surface at 10.4 KV

Figure 6.5 (h) Same surface at 12.0 KV

Figure 6.5 (i) Same surface at 13.8 KV

Figure 6.5 (j) Same surface at 16.0 KV

section 3.2) appears in Figure 6.5 (h) to (j).

With type (ii) corrosion, there was seen to be a streak from (111) through (110) to (1$\bar{1}$1), and continuous field corrosion was observed on the entire imaging surface. The field evaporation end form has a spike-like shape (Figure 6.5(g)). After field evaporation of this spike, the tip specimen had almost the same radius as it had before the treatment. Further field evaporation made it possible to show the entire tip surface. In Figure 6.5 (i) and (j), the corrosion fronts are observed around the edge of the imaging part of the tip, i.e., around peripherical (110) region, and show the type (i) corrosion in section 3.2.

Tungsten is hardlyoxidized by heating 400°C in air, then, this phenomena can be considered in terms of erosion and the redistribution of tungsten atoms.

Also, the main reactant in this corrosion process is considered to be oxygen and water molecules which are trapped during electrodeposition by the same reason mentioned in section 6.3.

CHAPTER 7

CONCLUSIONS

7.1 Results

It is impossible to observe the images of the thin zinc and zinc-oxide films, as these films evaporate well below the helium imaging voltage.

Images obtained in this experiment show the two types of field corrosion by adsorbates, such as oxygen and water molecules.

When the main reactant is only oxygen, the corrosion front exists on crystallographically rather specific sites on the tip surface. When the main reactant is oxygen and water molecules, the continuous changes in the topography of the tip surface are observed, as well as the "doubling" or streak effect on the (110) terrace area.

The main reasons for observing the corrosion process of the tungsten tip specimen are considered as follows:

(1) it is impossible to outgas the specimen after electrodeposition or its post-deposition oxidation, because the melting points of zinc and zinc-oxide are well below that of tungsten. The water molecules trapped during electrodeposition and the atmospheric absorbates are therefore presented during the imaging operation,

(2) vacuum conditions in the microscope chamber and/or the gas handling plant are rather poor, because of the impossibility of baking the system.

7.2 Suggestions for further work.

It is obvious that this microscope system is not suitable for thin film studies. A field ion microscope system which provides bake-out facilitaties and an ultra-high vacuum background pressure is required. The low background pressure of the system would allow the application of image gases with lower ionization potentials. This would facilitate an imaging of materials that have lower field evaporation fields, e.g., low melting point soft metals such as gold, zinc,etc.

When gases with low ionization potentials, e.g., Ne, Ar, are used, image intensification is required. A principle difficulty here is that the conversion efficiency of the ion energy into photons decreases very rapidly with increasing ion mass, most of the energy going into phonons, so that even external image intensifiers are almost useless for heavy mass ions. Hence an internal image intensifier such as a channel plate is required,because the ion/electron conversion efficiency is not a sensitive function of ion mass [56,57].

Further, it is desirable to work with as low a tip temperature as possible; this necessitates the use of liquid hydrogen or helium. The advantages of using these would be better resolution, higher brightness, and reduced background pressure[58].

Another very important point is that thin film manufacture should be carried out inside the micrscope chamber by means of thermal evaporation, mechanical contact, etc., so that elimination of contamination and outgassing of the specimen before deposition may be facilitated.

REFERENCES

1. G. Ehrlich, J. Chem. Phys. 36, 1171, 1962.
2. G. Ehrlich and F.G. Hudda, J. Chem. Phys. 36, 3233, 1962.
3. G. Ehrlich, Discussions Fraday Soc. 41, 7, 1966.
4. W.M. Sachtler and A.A. Holscher, Discussions Fraday Soc. 41, 29, 1966.
5. J.F. Mulson and E.W. Müller, J. Chem. Phys. 38, 2615, 1963.
6. S. Nakamura and E.W. Müller, J. Appl. Phys. 36, 3634, 1965.
7. R.T. Lewis and R. Gomer, Surface Sci. 26, 197, 1971.
8. G.K.L. Cranstowr and J.S. Anderson, Surface Sci. 35, 319, 1973.
9. L.I. Maissel and R. Glang, eds., "Handbook of Thin Film Technology", McGraw-Hill, New York, 1970.
10. H.M. Montagu-Pollock, T.N. Rhodin and M.J. Southon, Surface Sci. 12, 1, 1968.
11. A.J. Melmed, J. Appl. Phys. 38, 1444, 1965.
12. J.P. Jones, Proc. Roy. Soc. (London) A284, 469, 1965.
13. G.D.W. Smith, Surface Sci. 35, 304, 1973.
14. D.W. Bassett, Surface. Sci. 21, 181, 1970.
15. G.D.W. Smith and J.S. Anderson, Surface Sci. 24, 459, 1971.
16. E. Sugata, S. Ishii and K. Mastui, Surface Sci. 24, 612, 1971.
17. N.V. Durai Raghavan and B.J. Bayuzick, J. Vac. Sci. Technol. 9, 784, 1972.
18. T. Gurney, F. Hutchinson and R.D. Young, J. Chem. Phys. 42, 3939, 1965.
19. R.D. Young and D.C. Schubert, J. Chem. Phys. 42, 3943, 1965.

20. D.S. Whitmell, Surface Sci. 11, 37, 1968.

21. W.R. Graham, F. Hutchinson, J.J. Nadakarrkaren, D.A. Reed, and S.W. Schwenterly, J. Appl. Phys. 40, 3931, 1969.

22. W.R. Graham, D.A. Reed and F. Hutchinson, J. Appl. Phys. 43, 2951, 1972.

23. K.D. Rendulic and E.W. Müller, J. Appl. Phys. 38, 550, 1967.

24. O. Nishikawa and K.D. Rendulic, Surface Sci, 26, 677, 1971.

25. T. Utsumi and O.Nishikawa, Appl. Phys. Lett. 21, 110, 1972.

26. O. Nishikawa and T. Utsumi, J. Appl. Phys. 44, 945, 1973.

27. O. Nishikawa and T. Utsumi, J. Appl. Phys. 44, 955, 1973.

28. E.W. Müller, Z. Phys. 131, 136, 1951.

29. R. Gomer, "Field Emission and Field Ionization", Havard U. Press, Cambridge, 1961.

30. J.J. Hren and S. Ranganathan, eds., "Field Ion Microscopy", Plenum, New York, 1968.

31. E.W. Müller and T.T. Tsong, "Field Ion Microscopy", American Elsevier, New York, 1969.

32. K.M. Bowkett and D.A. Smith, "Field Ion Microscopy", North Holland, Amsterdam, 1970.

33. E.W. Müller and K. Bahadur, Phys. Rev. 102, 624, 1956.

34. E.W. Müller, Adv. Electronics and Electron Physics 13, 83, 1960.

35. R. Gomer and L.W. Swanson, J. Chem. Phys. 38, 1613, 1963.

36. P.J. Smith and D.A. Smith, Phil. Mag. 21, 907, 1970.

37. B.E. Conway and J.O.M. Bockris, Electrochem. Acta 3,340, 1961.

38. B.E. Conway and J.O.M. Bockris, Proc. Roy. Soc. (London) A248, 394, 1958.

39. K.L. Chopro, "Thin Film Phenomena", McGraw-Hill, New York, 1969.

40. K.R. Lawless, Physics of Thin Film, 4, 191, 1967.

41. V.I. Lainer, "Modern Electroplating", Israel Program for Scientific Translations, Jerusalem, 1970.

42. G.A. Rozganyi and W.J. Polito, App. Phys. Letters, 8, 220, 1966.

43. G.A. Tozganyi and W.J. Polito, J. Vac. Sci. Technol. 6, 115, 1969.

44. R.A. Mickelsen and W.D. Kingery, J. Appl. Phys. 37, 3541, 1966.

45. D.L. Raimondi and E. Kay, J. Vac. Sci. Technol, 7, 96, 1970.

46. G. Heiland, E. Mollow and F. Stöckmann, Solid State Physics, 8, 191, 1959.

47. R.R. Bair and L.J. Schustick, in "Modern Electroplating", ed., A.G. Gray, The Electrochemical Society, New York, 460, 1953.

48. W. Blum and B.B. Hegaboam, "Principle of Electroplating and Electroforming", McGraw-Hill, New York, 1949.

49. R.W.G. Wyckoff, "Crystal Structures", 2nd ed., John Wiley and Sons, New York, 1963.

50. W.L. Bragg and J.A. Darbyshine, Trans. Fraday Soc. 28, 522, 1932.

51. B. Gregov, M.Sc. Thesis, The University of Alberta, 1971.

52. R.C. Weast, ed., "Handbook of Chemistry and Physics, 52nd ed", Chemical Rubber Co., Ohio, 1972.

53. E.W. Müller, in: "Structure and Properties of Thin Films", eds., C.A. Naugebauer, J.B. Newkirk and D.A. Vermilyer, Wiley, New York, 476, 1959.

55. O. Nishikawa, A private communication.

56. P.J. Turner, P. Cartwright, M.J. Southon, A. Van Oostram and B.W. Manley, J. Sci. Instr. 2, 731, 1969.

57. R. Lewis and R. Gomer, Appl. Phys. Letters, 15, 384, 1969.

58. D.G. Brandon, in "High-temperature, High-resolution Microscopy", eds., H.I. Aarowson and G.S. Ansell, Goden and Breach, New York, 281, 1967.

59. A. Messiah, "Quantum Mechanics", Interscience Publishers, New York, 1962.